Effects of vortex formation and interaction on turbulent mass transfer over a two-dimensional wavy wall

Enwei Zhang [1], Wangxia Wu [2], Qingquan Liu [2,*] and Xiaoliang Wang [2,†]
[1] *Institute of Mechanics, Chinese Academy of Sciences, Beijing 100190, China*
[2] *School of Aerospace Engineering, Beijing Institute of Technology, Beijing 100081, China*

(Received 8 June 2022; accepted 24 October 2022; published 21 November 2022)

The present paper conducted a large-eddy simulation of turbulent flow and mass transfer over two-dimensional wavy walls with different wave slopes (ratio of amplitude to wavelength ranging from 0.0375 to 0.1) to investigate the generation and interaction of vortices and the effect on turbulent mass transfer. The present wavy wall induces flow separation and reconstructs a turbulent shear layer having a concave feature, and thus triggers streamwise vortices via the centrifugal instability mechanism. We confirm that these vortices originate from separation and reattachment points. The convex wall enhances the spanwise vorticity traced to the upstream trough, such that spanwise vortices form via the Kelvin-Helmholtz instability mechanism deviating from the crest. There are four vortex modes between crests controlling the turbulent scalar statistics. (1) The interaction between spanwise and streamwise vorticity activates strong shear, high-level turbulent kinetic energy (TKE) and Reynolds shear stress (RSS) near the separation point while upstreaming the origins of high streamwise and vertical turbulent scalar fluxes (VTSF). (2) The shear effect in the separation zone maintains the TKE and RSS, whereas the trapped separation bubble causes dominated scalar diffusion on the leeward side. (3) Vortex pairs are generated at the reattachment point to eject low-momentum and low-scalar fluids upward into the average flow. (4) The layout of vortices on the windward side is reversed to that in the separation point, and the restriction of the convex wall on the streamwise vorticity weakens the shear and forms a region of low RSS and VTSF.

DOI: 10.1103/PhysRevFluids.7.114607

I. INTRODUCTION

Turbulent flow over a wavy wall boundary can be found widely in nature, as seen for wind over waves and atmospheric boundary layer flow over wavy dunes. The wavy wall via generating kinds of vortices significantly affects the turbulent boundary layer flow and the process of mass transfer [1–4]. Therefore, an investigation of how wavy wall induces vortices and how they interact to govern the turbulent mass transfer would deepen the insight in clarifying the physical process of the interaction of the flow with the boundary and provide effective ways to control turbulent mass transfer.

Over the years, a large number of investigations have been conducted on the turbulent flow, including heat and mass transfer, over wavy walls [4,5–13]. In the wavy wall turbulence problem, the ratio of boundary layer thickness to the amplitude, Reynolds number, wave slopes, etc., are known to be the crucial parameters. The first parameter determines the forms of the wall boundary, which can be considered as roughness or obstacles. Jiménez [14] suggested that the ratio of the boundary layer thickness to the roughness height must meet the need of $\langle\delta\rangle/a \geqslant 40$ to achieve

*Corresponding author: liuqq@bit.edu.cn
†wangxiaoliang36@bit.edu.cn

outer-layer similarity. Therefore, this kind of wall boundary can be treated as roughness. That does not meet this requirement that $\langle\delta\rangle/a \geqslant 40$ is equivalent to flowing over an obstacle. In contrast, the Reynolds number and wave slopes jointly govern the flow regime, which is divided as separated or nonseparated flow [1]. Due to the common flow separation in wavy wall turbulence, studies focus more on this flow regime. As pointed out by Yoon *et al.* [15], the typical feature of the fluid across a wavy or dune-shaped wall was flow separation and reattachment phenomena. The flow separation behind the crest leads to the variation of momentum along the wavy wall, hindering the momentum transport and reducing the average flow velocity in the low momentum region, consequently, forming a feature where low momentum fluids cover the concave region [16]. After the flow separation, the reattachment of part of the separated shear layer (SSL) injects vorticity in the near-wall region into the recirculation zone [17,18], increasing the spanwise vorticity. In the process of flow reattachment, extensive vortices are generated. Angelis *et al.* [19] and Henn and Sykes [20] found that there are greater spanwise velocity fluctuations on the windward side of the wavy wall afterthe flow reattachment, and believed that is related to the streamwise vortices. These vortices, through their high kinetic energy, further affect momentum [21] and scalar transfer [22,23], which have been confirmed by Kruse and Von Rohr [24] and Bahaidarah *et al.* [16]. They pointed out that the instantaneously generated streamwise vortex appeared on the upslope part of the wavy wall and elevated the momentum and heat transfer. These investigations connected the relationship between vortices and momentum (scalar) transport and verified the important role of vortices in a variation of momentum. However, the role of how the vortices interact in modulating instantaneous quantity or statistics of turbulence is still unclear.

Due to the significance of vortices on the transportation of momentum (scalar), numerous studies have been carried out on the wavy wall's effect on the characteristics of different types of vortices. The horseshoe vortices, streamwise, and spanwise vortices are known to be the basic flow structures in a fully developed turbulent boundary layer. Omidyeganeh and Piomelli [25] pointed out that in the two-dimensional wavy wall (dune) turbulence, the flow structures are mainly derived from the Kelvin-Helmholtz instability of the SSL, which causes the spanwise vortex structure to experience lateral instability when advancing downstream and develops into a horseshoe vortex structure, with a size comparable to the flow depth [26,27]. This also implies that the horseshoe vortex structure is generated by the shedding vortices in the separated turbulent shear layer [28]. Moreover, the morphological variation of vortex structures governs the turbulent momentum (scalar) transfer. As noted by Kuhn *et al.* [29], the initially spanwise-oriented large coherent structures start to become streamwise oriented, and this flow reorganization is visible in the enhancement region of the local heat transfer. However, the features of streamwise vortices are more complicated, as shown by Zedler and Street [30], who conducted a numerical investigation of turbulent flow over a wavy surface and proposed that the internal distances of streamwise vortices are relatively far and dip angle is high, which may determine the momentum away from the wall. These studies gave details of the vortex's features and qualitatively interpreted the likely mechanism of vortices formation. Whereas the specific mechanism of how a wavy wall induces the formation of streamwise vortices and where might be the origin of these vortices are remained to be revealed.

The interaction between various vortices on the wavy wall would induce a strong shear effect, which has a significant impact on the turbulent stress of the flow field. Hossain and Islam [31] reported the important roles of the flow structures above a wavy wall. The vortex structures form under a strong turbulent shear condition, but Mahmud *et al.* [32] reported that the wall shear stress is weak near the convex surface of a wavy wall. In flow across a wavy wall, the streamwise component of the shear stress reduces, whereas the spanwise component increases, which is related to the spanwise rotating motion induced by vortex pairs. The interaction of these vortex pairs promotes momentum transfer from the near-wall region to the core region of the flow, thus enhancing the momentum (scalar) transfer [33]. The wavy wall destroys the coherent structure near the wall, forming different types of vortex structures that lead to complex turbulent fluctuations and thus reduce the peak value of the Reynolds normal stress profile from the view of the time-averaged field [34,35]. Moreover, Yang and Shen [36] suggested that the momentum (scalar) is governed by the

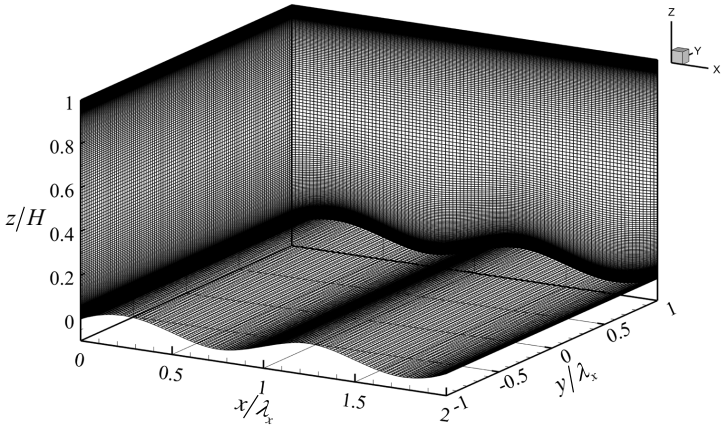

FIG. 1. Physical model and grid distribution of the computational domain for case C2.

joint effect of the characteristic vortex structure and its priority position, which further supports the important effects of vortex interaction on momentum and scalar transports. However, there is still a lack of sufficient understanding of the connection between vortex interaction and the turbulent statistics when flowing over a wavy wall, such as how different vortices interact to enhance or maintain high-level turbulent stress, or how the vortex interaction affects the scalar transfer.

The above-mentioned investigations provide a deep understanding of vortex structures above a two-dimensional wavy wall. From the shortcomings of existing research, there remain some questions, including (a) How do the streamwise vortices generate, and where might be the origins of these kinds of vortices above a two-dimensional wavy wall? (b) What dominates the spanwise vorticity production? (c) How do different types of vortices interact to produce a variation of turbulent mass statistics? Based on these motivations, this paper discussed the mechanism of vortex formation and interaction as well as the effects on high-order statistics via large-eddy simulation (LES) of turbulent mass transfer above a two-dimensional wavy wall. The remainder of the manuscript is organized as follows. Sections II and III describe the physical model and numerical methodology. Section IV gives the formation mechanism of the streamwise vortices, and Sec. V confirms the generation of the spanwise vortex. Section VI emphasizes the effects of vortex interaction on the statistics of turbulent mass transfer. The main conclusions are then summarized in Sec. VII.

II. PHYSICAL MODEL

To investigate the wall effect on the formation and interaction of vortices, the wavy wall constructed in the present paper is expressed as $\eta = a\sin(2\pi x/\lambda_x)$ (where a is the wave amplitude and λ_x is the wavelength), as shown in Fig. 1. The shape can be characterized by a/λ_x (wave slope). As shown in Table I, six cases with different wave slopes ranging from 0.0375 to 0.1 are

TABLE I. Parameter settings for different cases.

Case	Δx^+	Δy^+	Δz^+_{wall}	a/λ_x	$\langle\delta\rangle$/m	Re	Sc
C1	11.5	11.5	0.57	0.0375	0.02754	4000	0.7
C2	12.8	12.8	0.64	0.05	0.027902		
C3	15.2	15.2	0.76	0.0625	0.032315		
C4	17.5	17.5	0.87	0.075	0.03509		
C5	18.4	18.4	0.92	0.0875	0.03592		
C6	19.9	19.9	0.99	0.1	0.03468		

simulated (with the wavelength fixed while the amplitude is varied). The computational domain is $(x/\lambda_x, y/\lambda_x, z/H) = (2, 2, 1)$, where $H = 1.125\lambda_x$ is the channel height. The domain is thought to be sufficiently large to capture turbulent structures based on the two-point spatial correlation [35,37,38].

III. NUMERICAL METHODOLOGY

A. LES model

An LES was conducted to simulate the turbulent mass transfer above a two-dimensional wavy wall. The filtered three-dimensional incompressible Navier-Stokes equations and scalar transport equation in Cartesian coordinates are

$$\frac{\partial u_i}{\partial x_i} = 0, \tag{1}$$

$$\frac{\partial u_i}{\partial t} + u_j \frac{\partial u_i}{\partial x_j} = -\frac{1}{\rho}\frac{\partial p}{\partial x_i} + \nu \frac{\partial^2 u_i}{\partial x_j \partial x_j} - \frac{\partial \tau_{ij}}{\partial x_j} + \Pi \delta_{1i}, \tag{2}$$

$$\frac{\partial \theta}{\partial t} + u_j \frac{\partial \theta}{\partial x_j} = D \frac{\partial^2 \theta}{\partial x_j \partial x_j} - \frac{\partial \tau_j^\theta}{\partial x_j}, \tag{3}$$

where $x_i (i = 1, 2, 3) = (x, y, z)$ denotes the streamwise, spanwise, and vertical coordinates, $u_i (i = 1, 2, 3) = (u, v, w)$ denotes the filtered velocity components, p is the filtered pressure, θ is the filtered scalar, Π is the external force transformed as the pressure gradient driving the flow, δ_{ij} is the Kronecker delta, ρ is the density, ν is the kinematic viscosity, D is the molecular diffusion coefficient, and τ_{ij}, τ_j^θ, respectively, represent the subgrid-scale stress tensor and subgrid-scale scalar flux. In the present study, the dynamic one-equation is used as a subgrid-scale model [39]. The subgrid-scale scalar flux can be determined using the simple gradient hypothesis, $\tau_j^\theta = \frac{\upsilon_s}{Sc}\frac{\partial \theta}{\partial x_j}$.

B. Simulation configuration

The turbulent flow is driven by an external force transformed as the pressure gradient that varies with time to obtain the fixed bulk velocity, with periodic conditions applied along the streamwise and spanwise directions and no-slip boundary conditions applied to the upper and bottom walls. The Reynolds number based on the bulk velocity and half height of the channel is $\mathrm{Re} = U_0 h/\nu = 4000$, which provides fully developed turbulence. For scalar transport, we set the initial scalar of the fluid as $\theta_0 = 2$ with the Dirichlet boundary condition $\theta_{\mathrm{wall}} = 0$ imposed on the upper and bottom walls, which is similar to that used by Michioka [40].

The grid points are evenly spaced in both streamwise and spanwise directions as shown in Fig. 1. In the vertical direction, the grid points are clustered at the boundary through an exponential transformation with the first grid point meeting the need of $\Delta z^+_{\mathrm{wall}} < 1$ to enhance the accuracy of the boundary layer. The total number of grid points in this paper is $N_x \times N_y \times N_z = 101 \times 101 \times 181$. The dimensionless grid scale is presented in Table I. The mesh system should be carefully validated for scalar transport because the order of the ratio of the Kolmogorov scale to the Batchelor dissipative scale is $Sc^{-1/2}$ (i.e., the negative half-power of the Schmidt number, which is the ratio of the molecular diffusion coefficient to the kinematic viscosity) [41–43]. The Schmidt number $\mathrm{Sc} = 0.7$ is considered in the present study. Therefore, the same mesh system can be used for both momentum and scalar transport. The boundary layer thickness $\langle \delta \rangle$ (with the brackets denoting spatially averaged conduction along both the spanwise and streamwise directions) in Table I refers to the spatially averaged vertical distance when the temporally averaged velocity reaches 99% of the bulk velocity. It is noted that the ratio of boundary layer thickness to amplitude is varied by approximately 10, which means that the wall boundary can be treated as an obstacle. Therefore, the present paper does not pay attention to the roughness regime.

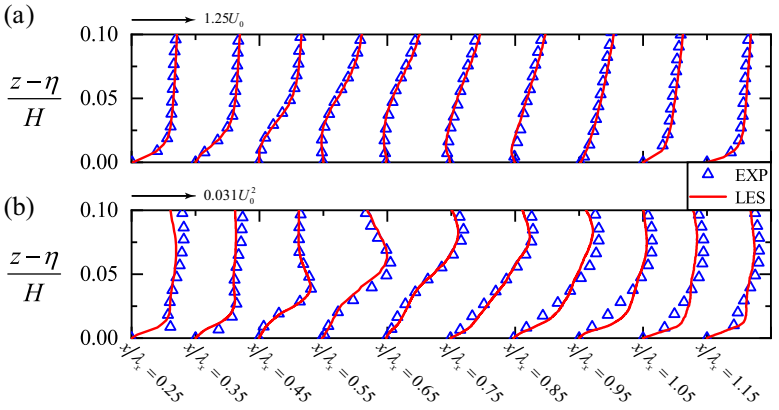

FIG. 2. Comparison of the present simulation results and the experimental results obtained by Hamed *et al.* [12]: (a) time-averaged streamwise velocity profiles along one wavelength and (b) turbulent kinetic energy profiles along one wavelength. Blue triangles are the experiment results (EXP) and red solid lines are the present simulation results (LES).

The second-order backward implicit time advancement scheme was used for the time update, and the convection term was discretized using a second-order upwind difference scheme. The finite volume method based on the standard pressure-velocity coupling and PIMPLE algorithm, which is a variant of the PISO method, is used to solve the governing equations. The PIMPLE algorithm combines the idea of SIMPLE (semi-implicit method for pressure-linked equations) and the PISO algorithm and regards each time step as a steady-state flow. When the solution is obtained according to the steady-state algorithm to a certain extent (here we set two loops of the iterative solutions), the standard PISO algorithm is used for the last step.

C. Verification of the numerical model

To verify the numerical model, we simulated one case of the experiment conducted by Hamed *et al.* [12] (with the parameter settings given in Table I as case C2). Fig. 2 shows that the mean velocity profile agrees well with that obtained by Hamed *et al.* [12]. For high-order statistics, such as turbulent kinetic energy ($\frac{1}{2}\overline{u_i' u_i'}$, where the overline denotes time-averaged conduction) shown in Fig. 2(b), the present results are in basic agreement with the experimental results.

It is noted that we focus on the resolved quantity without the subgrid-scale quantity. The subgrid-scale quantity should be evaluated meticulously in LES. In the present study, we found that the subgrid-scale quantity is approximately two orders of magnitude less than the resolved quantity (shown in Fig. 3), and we thus ignored its effect. In fact, by evaluating the dimensionless grid scale given in Table I, we find that the present LES is approximately equivalent to a quasi-direct numerical simulation. Therefore, the results in the present simulation are reliable.

IV. FORMATION AND SPATIAL DISTRIBUTION OF GÖRTLER VORTICES

A. Potential region of centrifugal instability

In the case of turbulent flow over a curved wall, the streamlines curved through the wall, which can induce centrifugal instability. This section tries to investigate the likely formation mechanism of streamwise vortices related to centrifugal instability. The potentially unstable region can be characterized by the Rayleigh criterion [44,45]

$$\varphi_{xz} = \frac{2|\bar{\mathbf{u}}|\bar{\omega}_y}{R_y}, \tag{4}$$

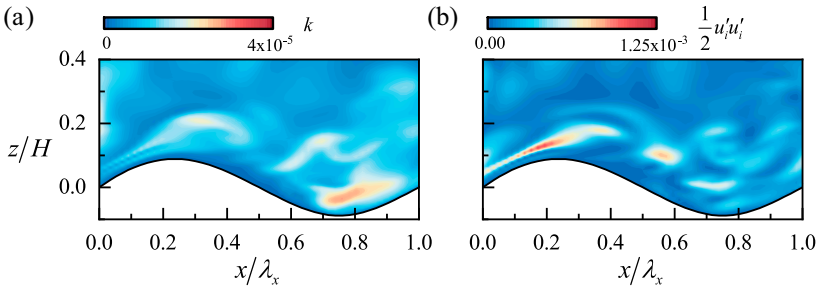

FIG. 3. Comparison of the instantaneous (a) subgrid-scale kinetic energy k and (b) resolved turbulent kinetic energy $\frac{1}{2}u_i'u_i'$ for case C6. The former is approximately two orders of magnitude lower than the latter. Note that the dimensionless grid scale is the largest for C6. Consequently, the subgrid-scale quantity can be ignored in all cases.

where $|\bar{\mathbf{u}}|$ is the modulus of the time-averaged velocity and $\bar{\omega}_y$ is the spanwise vorticity. R_y is the local algebraic radius of curvature based on the time-averaged velocity vector $(\bar{u}, \bar{w})$, which is calculated by $R_y = |\bar{\mathbf{u}}|^3/(\bar{u}a_z - \bar{w}a_x)$, where a_x, a_z are the components of convective acceleration calculated from $(\bar{\mathbf{u}} \cdot \nabla)\bar{\mathbf{u}}$. According to the Rayleigh criterion, the flow could be unstable if the sign of the local radius of curvature is the reverse of the sign of the vorticity.

Figures 4(a)–4(f) illustrates the potentially unstable region characterized by the Rayleigh criterion for all cases and the time-averaged velocity vector $(\bar{u}, \bar{w})$. A blue solid line in the figure shows the isoline of $\varphi_{xz} = -2$, whereas a red solid line shows $\bar{u} = 0$. The main potential unstable region appears in the reattachment region, which is attributed to the high curvature of the turbulent shear layer that stimulates centrifugal instability. In addition, there is a tiny potential unstable region near the separation point and trough, the former region is due to the curved streamline effect above the separation bubble [46] that is similar to that of a concave wall boundary in the generation of Görtler vortices, whereas the latter region is due to the reversed flow over the real concave trough that

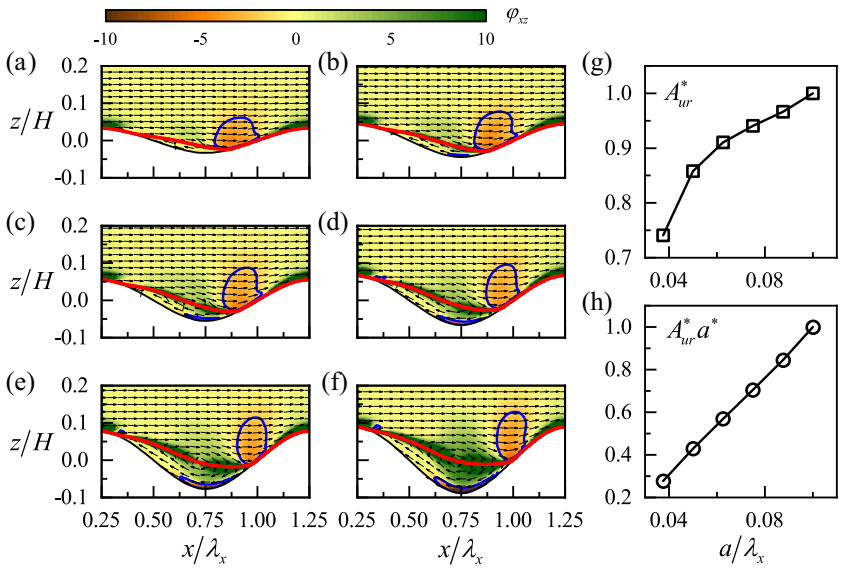

FIG. 4. (a)–(f) Contour of φ_{xz} based on the Rayleigh criterion for all cases. The time-averaged velocity vector $(\bar{u}, \bar{w})$ is shown by the arrows. Solid blue lines represent isolines of $\varphi_{xz} = -2$. Solid red lines show $\bar{u} = 0$. (g), (h) Normalized area of the unstable region as a function of the wave slope.

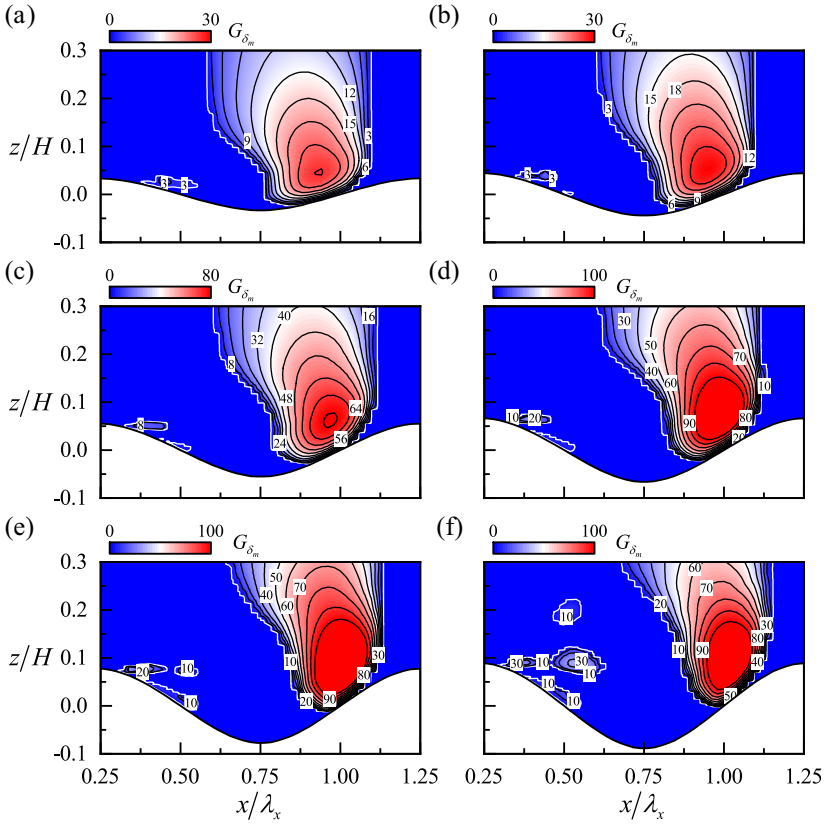

FIG. 5. (a)–(f) Distribution of the Görtler number based on the momentum thickness of the boundary layer. The white solid lines represent the critical value of Eq. (6).

might induce centrifugal instability. Figure 4(g) shows the normalized area A^*_{ur} ($A_{ur} = \int_S dS$, where S is the enclosed region by $\varphi_{xz} = -2$) as a function of the wave slope (where an asterisk indicates normalization by the maximum value among the six cases). Moreover, Fig. 4(h) gives the results of $A^*_{ur}a^*$ for all cases, where a^* is the normalized wave amplitude (normalized by the maximum wave amplitude for all cases). It shows that an increase in the wave slope leads to a large area with potential instability. This arises because flow separates more readily for the large wave slope, and centrifugal instability occurs more readily for a steeper SSL with high curvature.

B. Görtler number

The Rayleigh criterion gives the necessary conditions for centrifugal instability while ignoring the stability condition contributed by the viscous effect. Therefore, we directly calculate the Görtler number to evaluate the ratio of the centrifugal effects to the viscous effects. The Görtler number is calculated from the momentum thickness of the boundary layer:

$$G_{\delta_m} = Re_{\delta_m}\left(\frac{\delta_m}{R_y}\right)^{1/2} = \frac{|\bar{\mathbf{u}}|\delta_m^{3/2}}{\nu R_y^{1/2}}, \tag{5}$$

where δ_m is the momentum thickness of the boundary layer, which can be determined by $\delta_m = \int_0^\infty \langle\bar{u}(z)\rangle(U_0 - \langle\bar{u}(z)\rangle)/U_0^2 dz$. The Görtler vortices would form once the curvature is large enough to follow the instability criterion. If we refer to Tobak [47] and Inger [48], the criteria and critical

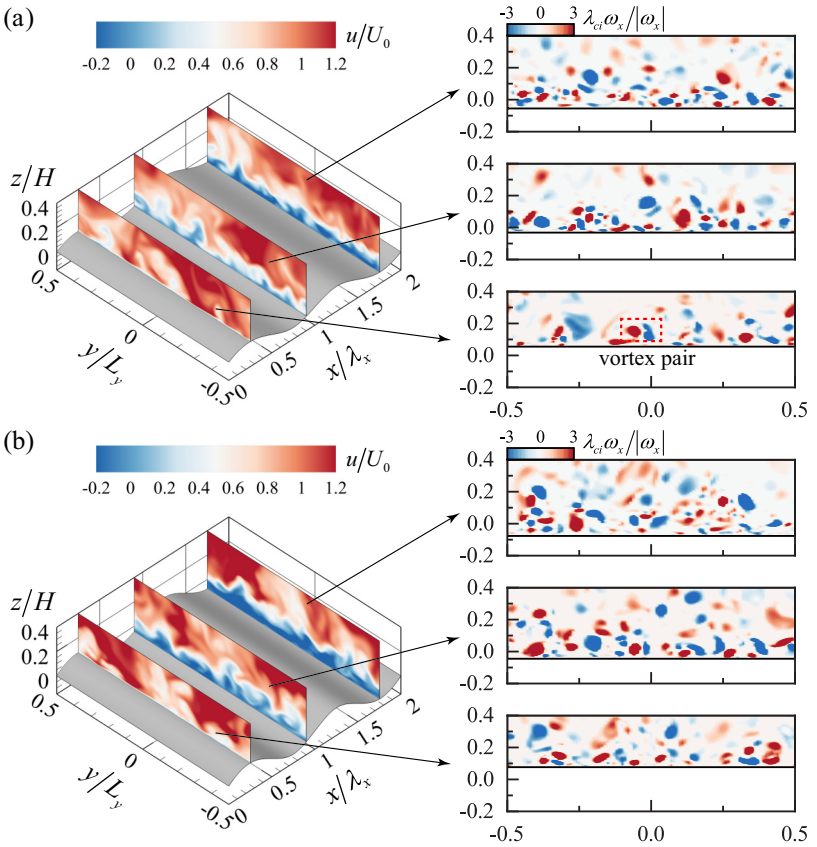

FIG. 6. Instantaneous swirling strength at different cross sections for (a) case C3 and (b) case C5.

values are expressed as follows:

$$G_{\delta_m} = \frac{|\bar{\mathbf{u}}|\delta_m^{3/2}}{\nu R_y^{1/2}} \geqslant 0.25. \tag{6}$$

Figure 5 shows the distribution of the Görtler number based on Eq. (5). Figure 5(a) shows that high G_{δ_m} appears at $x/\lambda_x \approx 0.9$ on the windward side and expands vertically. The region of high G_{δ_m} corresponds to the trough of the isoline of $\bar{u} = 0$ as shown in Fig. 4. As shown in Fig. 5, the range of high G_{δ_m} increases with the wave slope, and the higher wave slope results in higher G_{δ_m} on the windward side. However, the region with higher G_{δ_m} on the windward side will shift slightly downstream as the wave slope increases, as shown in Figs. 5(a)–5(f). We integrate the Görtler number in the potentially unstable region on the windward side (i.e., the region enclosed by the isoline of $\varphi_{xz} = -2$, as shown in Fig. 4) for case C1 to obtain the local averaged Görtler number. We find that $\int_{A_{ur}} G_{\delta_m} dA_{ur} \approx 19.95 \gg 0.25$, suggesting the occurrence of centrifugal instability and that the threshold condition of Görtler vortices has been exceeded. Additionally, near the separation point, G_{δ_m} meets the threshold condition, which indicates another origin of Görtler vortices. It is noted that the integral over the unstable region aims to obtain the local averaged instability. As shown in Fig. 5, G_{δ_m} exceeds the threshold condition near the separation and reattachment points. Therefore, the separation and reattachment points are the origins of Görtler vortices (or streamwise vortices).

C. Swirling strength at different cross sections

Furthermore, the streamwise vortices' swirling strength and spatial variance are discussed. Here, the component of the swirling strength λ_{ci} is defined as the imaginary part of the complex eigenvalue of the velocity gradient tensor [49]. We depicted the direction of the swirl, either clockwise or anticlockwise by multiplying the sign of the streamwise vorticity.

Figure 6 shows the instantaneous streamwise velocity and swirling strength at different cross sections ($x/\lambda_x = 0.25, 0.9, 1.75$) for cases C3 and C5. We see that a large-scale swirl appears in the near-wall region, centralizing below the region $z/H < 0.3$. Fig. 6(a) shows that at the section $x/\lambda_x = 0.25$, the vortices with clockwise and anticlockwise motions assemble as the vortex pair shown in the red dashed box. This kind of vortex pair induces upwash or downwash motion which is ubiquitous for the Görtler vortices, as reviewed by Floryan [50]. Moreover, the present streamwise vortices agree with Calhoun and Street [51], who believed that the streamwise vortices are linked to a Görtler instability mechanism. At the section $x/\lambda_x = 0.9, 1.75$, the vortices are distributed with greater concentration and stronger swirls. The high strength of streamwise vortices affects the momentum transport by weakening the streamwise momentum transfer. Figure 6(a) also shows an apparent momentum deficit in the near-wall region in the distribution of the instantaneous streamwise velocity. When increasing the wave slope, as shown for case C5 in Fig. 6(b), there is a clearly enhanced and centralized swirl. Taking section $x/\lambda_x = 0.9$ as an example, the swirling strength is higher for case C5 than case C3, and consequently, on the central line of the vortex pair, a higher swirl ejects the low-momentum fluid upward into the instantaneous flow more easily and transfers the upper high-momentum fluid into the near-wall region on the other side of the streamwise vortex. This process leads to a lifted low-momentum fluid, and the low-momentum region with a momentum deficit thus expands vertically. In a flow period, owing to the momentum balance, the momentum deficit of the near-wall region induces a momentum surplus at a higher vertical position, which is reflected in the high instantaneous streamwise velocity far from the wall.

To quantitively evaluate the wave slope effect, we integrate the time-averaged swirling strength at crest and trough cross sections for all cases in the active region to obtain its variance as a function of the wave slope. The integrated time-averaged swirling strength, namely the mean swirling strength I_{ci}^{+}, is obtained as

$$I_{ci}^{+} = \frac{1}{A_{yz}} \int_{-0.5L_y}^{0.5L_y} \int_{\eta(x,z)}^{\delta} |\bar{\lambda}_{ci}\langle\delta\rangle/U_0| dy dz, \tag{7}$$

where A_{yz} is the integration region and the ranges in spanwise and vertical directions are $y \in [-0.5L_y, 0.5L_y]$ ($L_y = 2\lambda_x$ is the spanwise length of the domain) and $z \in [\eta(x,z), \delta]$. Here, δ denotes the boundary layer thickness without spatial-averaging conduction, which varies along the streamwise direction. The present study uses I_{ci}^{+} to quantify the strength of streamwise vortices produced in the turbulent boundary layer.

Figures 7(a) and 7(b) show the mean swirling strength I_{ci}^{+} at the crest and trough cross sections as a function of the wave slope. It is seen that the mean swirling strength increases with the wave slope. We calculate the mean swirling strength at different cross sections to obtain the variance along the streamwise direction, as shown in Fig. 7(c). The integrated swirling strength is expressed as

$$I_{ci}^{la} = \frac{1}{A_{yz}} \int_{-0.5L_y}^{0.5L_y} \int_{\eta(x,z)}^{\delta} |\bar{\lambda}_{ci}\delta/U_0| dy dz. \tag{8}$$

In contrast with Eq. (7), the swirling strength is made dimensionless by δ (without spatial averaging). Figure. 7(c) presents the streamwise variance curves of I_{ci}^{la}, with a peak value appearing at $x/\lambda_x = 0.9$ due to the large-scale strengthened streamwise vortices as shown in Fig. 7(e) for case C3, which corresponded to the potentially unstable region (or the latter origin of the streamwise vortices). After the peak, the mean swirling strength I_{ci}^{la} decreases to a minimum at $x/\lambda_x = 1.15$. Figure 7(d) is also related to case C3, which shows that the position of $x/\lambda_x = 1.15$ corresponds to the stable region identified using the Rayleigh criterion with $\varphi_{xz} > 0$. This correspondence

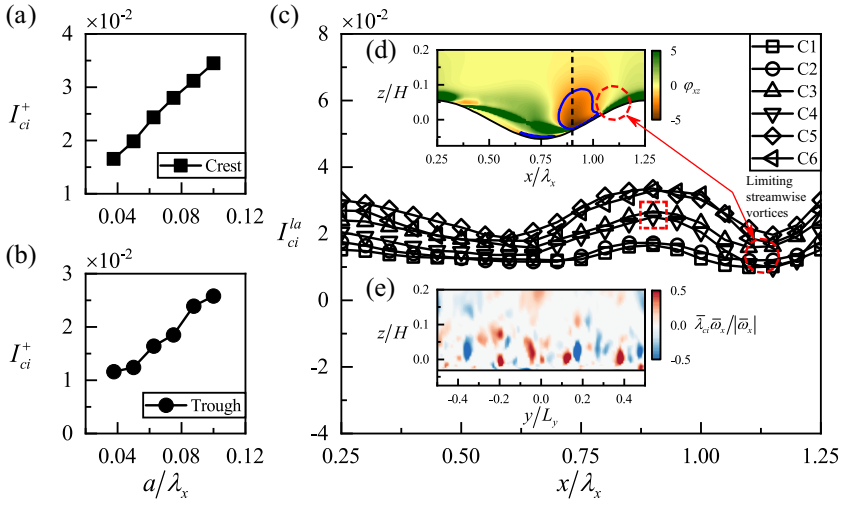

FIG. 7. (a) Mean swirling strength at crest cross sections and (b) mean swirling strength at trough cross-sections as a function of the wave slope. (c) The spatial variance of the mean swirling strength along the streamwise direction for all cases. (d) Contours of the results obtained using the Rayleigh criterion for case C3. (e) Swirling strength at $x/\lambda_x = 0.9$ for case C3.

is attributed to the convex-curvature and zero-curvature walls having a stabilizing effect on the pre-existing Görtler vortices generated by the concave curvature [52].

V. KELVIN-HELMHOLTZ INSTABILITY FOR GENERATING A SPANWISE VORTEX

A. Profiles of the vertical gradient of the streamwise velocity

As can be seen in Fig. 8, the flow separation reconstructs the $\bar{u} = 0$ (red dashed lines) that have the wavy feature out phase with the wall. The boundary layer results in a negative gradient near the leeward side that is attributed to the effect of reversed flow. Moreover, the gradient varies strongly near the isolines of $\bar{u} = 0$, which provides a strong shear effect on maintaining the recirculation. Furthermore, when the flow reattaches, the strong convection concentrates on the windward side, leading to a high gradient. Bennett and Best [27] proposed that the Kelvin-Helmholtz instability in the shear layer behind the crest is more likely to lead to macroscale turbulence above the wavy wall (dune) than the rupture of the wall turbulent boundary layer. This instability mechanism generates spanwise vortices in the SSL, which develop into horseshoe vortices through lateral instability during downstream advection [25]. We find that there is an inflection point with the maximum average gradient in the boundary layer profile, and this inflection point promotes flow instability [53].

The effect of the wave slope is reflected in the change in the spatial curvature of the turbulent shear layer, the peak value of the velocity gradient, and the spatial layout. The change of wave slope may change the positions of the separation point and reattachment point. The reattachment point in case C6 in Fig. 8(b) is shifted downstream compared with that in case C1, which results in strong shear appearing in a higher vertical position. In addition, as can be seen in Fig. 8, there is an obvious decrease in velocity gradient for a large wave slope case. This might be related to the wall-induced separation lowering the shear effect between the flow and the bounded wall.

B. Production of the spanwise vorticity

Spanwise vorticity can also be produced by the reorganization of the flow structures. As pointed out by Kuhn *et al.* [29], the initially spanwise-oriented large coherent structures start to become

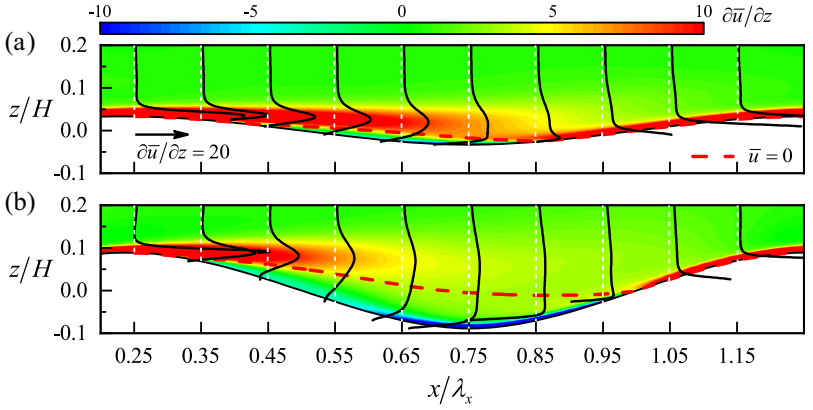

FIG. 8. Layout for $\bar{u} = 0$ and the profiles of the vertical gradient of the streamwise velocity (black solid lines) at different streamwise positions for cases (a) C1 and (b) C6. The white dashed lines represent the reference axis at different streamwise positions. The black solid lines extending into the wavy walls mean the vertical gradient in the wall boundary is quite strong, especially on the windward side.

streamwise-oriented when experiencing strong shear in wavy wall turbulence. Therefore, to further investigate the production of the spanwise vorticity, we solve the curl of the momentum equation, which is expressed as

$$\frac{\partial \omega_i}{\partial t} + u_j \frac{\partial \omega_i}{x_j} = \omega_j S_{ij} + \nu \frac{\partial^2 \omega_i}{\partial x_j \partial x_j}, \tag{9}$$

where $\omega_i = (\omega_x, \omega_y, \omega_z)$ is the vorticity vector. Through temporal averaging, Eq. (9) becomes

$$\frac{\partial \bar{\omega}_i}{\partial t} + \bar{u}_j \frac{\partial \bar{\omega}_i}{x_j} = \bar{\omega}_j \bar{S}_{ij} + \overline{\omega'_j S'_{ij}} - \frac{\partial \overline{u'_j \omega'_i}}{\partial x_j} + \nu \frac{\partial^2 \bar{\omega}_i}{\partial x_j \partial x_j}. \tag{10}$$

The first term on the right-hand side of Eq. (10) denotes the vorticity production due to the average strain effect. Here, we focus on the spanwise vorticity production $\bar{P}_{\omega y}$, which can be decomposed into three terms $\bar{P}_{\omega y} = \bar{\omega}_x \bar{S}_{xy} + \bar{\omega}_y \bar{S}_{yy} + \bar{\omega}_z \bar{S}_{zy}$ where $\bar{\omega}_x \bar{S}_{xy}$ ($\bar{\omega}_z \bar{S}_{zy}$) denotes the streamwise (vertical) vorticity transformed into spanwise vorticity under the strain effect of $\bar{S}_{xy}$ ($\bar{S}_{zy}$), whereas $\bar{\omega}_y \bar{S}_{yy}$ represents the growth of spanwise vorticity due to the strain effect of $\bar{S}_{yy}$. It is noted that the current mean flow is homogeneous in the spanwise direction, but it is spatially varied along the spanwise direction. Therefore, $\bar{S}_{yy}$ varied in the spanwise direction. Figure 9 shows the time-averaged dimensionless spanwise vorticity production contour for case C3 (made dimensionless by U_0, λ_x). The total spanwise vorticity production has an enhanced region near the separation point, extending downstream with the SSL. By calculating the components of spanwise vorticity production, it is seen that $\bar{\omega}_y \bar{S}_{yy}$ dominates production, whereas $\bar{\omega}_x \bar{S}_{xy}$ and $\bar{\omega}_z \bar{S}_{zy}$ contribute only 4% of the total production, as shown in Figs. 9(b)–9(d). This indicates that the spanwise vorticity is mainly generated by the growth of spanwise vorticity (induced by the Kelvin-Helmholtz instability of the SSL) and not by the transformation from streamwise or vertical vortices.

Figure 10(a) illustrates the time-averaged spanwise vorticity contour for case C3. As the spanwise vortex is produced mainly by the growth of spanwise vorticity, the local averaged production of the vorticity can be evaluated by integrating the production in the region under a certain isoline. As shown in Fig. 10(b), the local averaged spanwise vorticity production $\beta = \int_\Lambda \bar{\omega}_y^+ \bar{S}_{yy}^+ d\Lambda$ related to different cases is given, where Λ is the region enclosed by $\bar{\omega}_y = 10$. We also conducted integration in the region enclosed by $\bar{\omega}_y = 5$ and $\bar{\omega}_y = 1$. The results show that β is dependent on the chosen of $\bar{\omega}_y$. It is easy to know that as the integration region enlarges (equivalent to the decreases of $\bar{\omega}_y$),

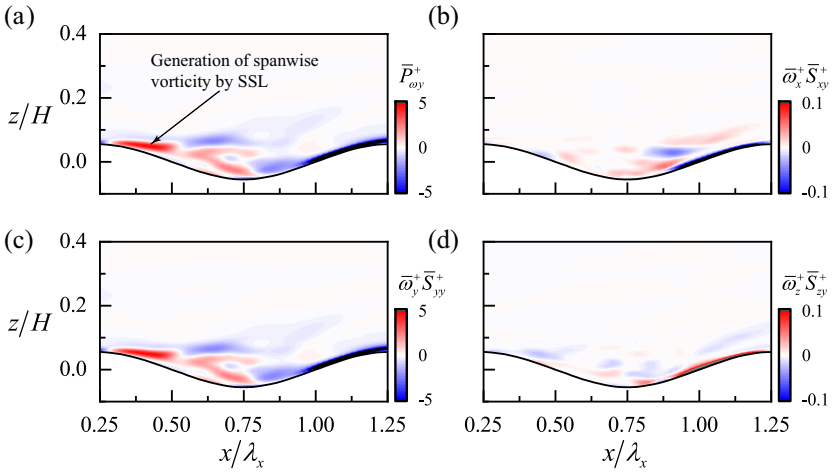

FIG. 9. Production of the spanwise vorticity for case C3: (a) total production, (b) production transformed from streamwise vorticity by $\bar{S}_{xy}$, (c) increase in spanwise vorticity due to $\bar{S}_{yy}$, (d) production transformed from vertical vorticity by $\bar{S}_{zy}$.

the local averaged spanwise vorticity production decreases. This is due to the enhanced production mainly located in the near wall region. Here we chose the region enclosed by $\bar{\omega}_y = 10$ because it includes almost regions near the separation point. The β increases positively with the wave slope. For small wave slopes as shown in Fig. 10(b), the growth rate is higher. The growth rate is lower when a/λ_x reaches 0.0625. Generally, the local averaged production of spanwise vorticity varies logarithmically with the wave slopes.

VI. EFFECT OF VORTEX INTERACTION ON THE STATISTICS OF TURBULENT MASS TRANSFER

A. Morphological features of vortex structures

The morphological features of vortex structures can be directly recognized by visualizing the instantaneous vortex structures. Figure 11(a) presents the instantaneous vortex structures obtained

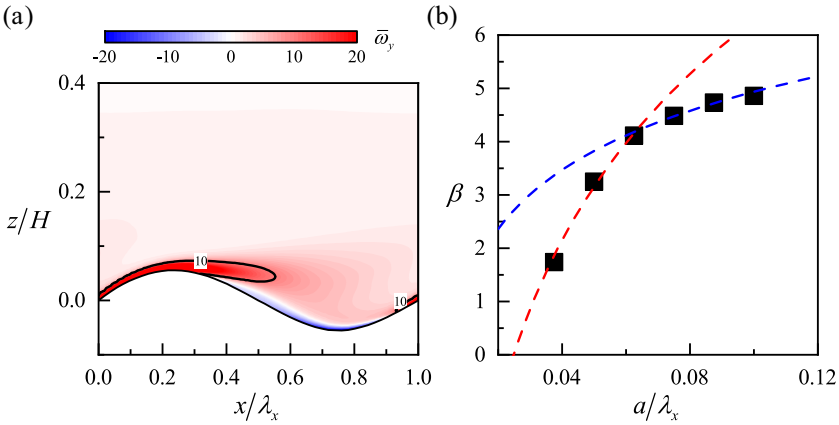

FIG. 10. (a) Time-averaged spanwise vorticity contour for case C3. (b) The local averaged spanwise vorticity production as a function of the wave slope.

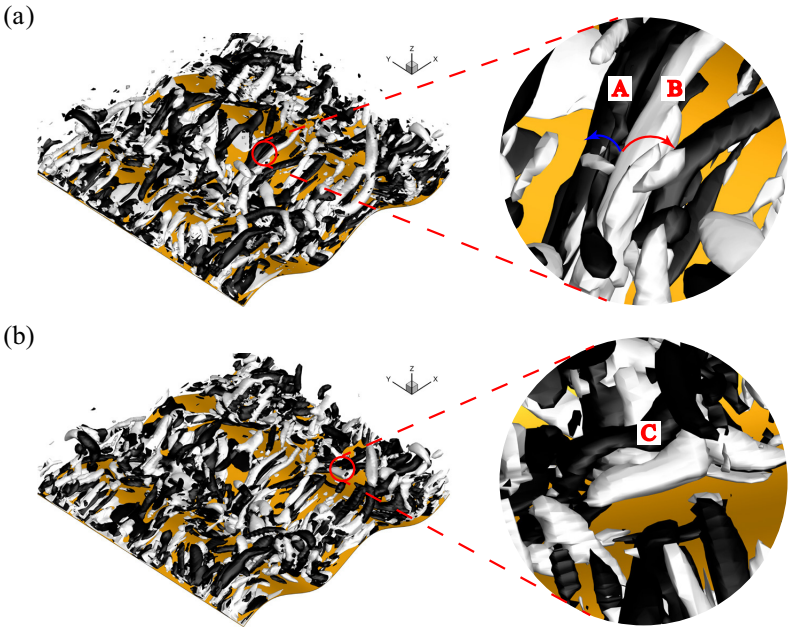

FIG. 11. Instantaneous vortex structures visualized using $\lambda_2 = -10$ for case C5. (a) Vortex structures with white for $\omega_x > 0$ and black for $\omega_x < 0$. (b) Vortex structures with white for $\omega_y > 0$ and black for $\omega_y < 0$.

using the λ_2 method [54] for case C5. The vortex structures are shown by the isosurface $\lambda_2 = -10$. In Fig. 11(a), the vortex structures were visualized by multiplying the instantaneous streamwise vorticity with white for $\omega_x > 0$ and black for $\omega_x < 0$. Figure 11(b) shows the vortex structures visualized by multiplying the instantaneous spanwise vorticity with white for $\omega_y > 0$ and black for $\omega_y < 0$. A large number of streamwise vortices are concentrated on the windward side [e.g., A and B in Fig. 11(a)] assembling as vortex pairs. These vortices gradually form vertically bent features as they extend downstream, which was also observed by Yang and Shen [55].

Figure 11(b) shows that typical spanwise vortices appear near the separation point (e.g., vortices C). The formation of spanwise vortices is highly related to the SSL. As illustrated in Fig. 8, the SSL behind the crest induces Kelvin-Helmholtz instability, which leads to spanwise vortices while the flow deviates from the crest.

The instantaneous vortex field also indicates the likelihood of interaction such as the upwelling motion by the vortex pairs. To emphasize the statistical vortex interactions, we further obtain the streamwise vorticity production to investigate the possible mechanism of the interaction between streamwise and spanwise vorticity. As shown in Fig. 12, the productions of (a) the spanwise vorticity and (b) the streamwise vorticity for case C3 are given. It is noted that the flow is strong three-dimensional, disturbed by the spanwise fluctuations. Therefore, the flow properties cannot be totally the same in every two wavelengths. As shown in Fig. 12(b), there are two regions with obvious streamwise vortices enhancement, which corresponded to the separation and reattachment points respectively. This further verifies the centrifugal instability mechanism for generating the streamwise vortices. Additionally, as shown in Fig. 12, a phase difference of approximately $\frac{\lambda_x}{8}$ between the activation region of these two vortices can be observed. This phase difference is universal and approximately unchanged with the wave slope. As the above discussions, the separation and reattachment points possess enhanced vorticity productions where the centrifugal instability induces streamwise vortices. The near separation region has an enhanced production where the K-H instability induces spanwise vortices. These positions indicate the origins of these vortices. Due to

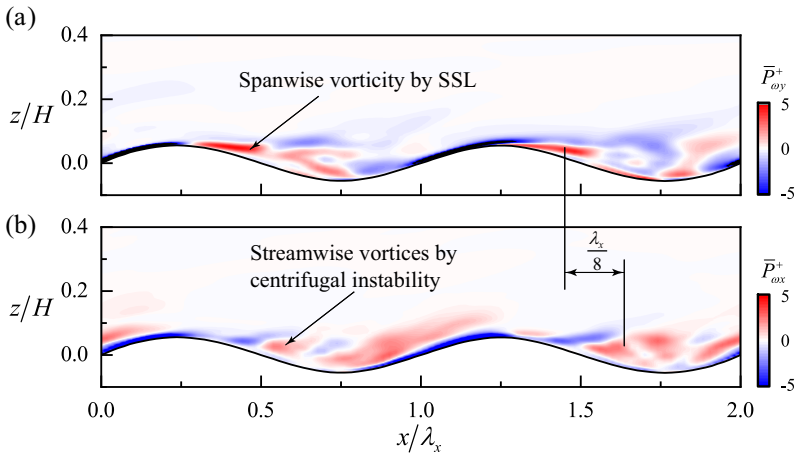

FIG. 12. (a) Production of the spanwise vorticity for case C3 and (b) production of the streamwise vorticity for case C3.

the slight effect of wave slope on the variation of separation and reattachment points, the phase difference is thus approximately unvaried. Figure 12 also shows the typical spatial layout of upward spanwise vorticity and downward streamwise vorticity.

B. Correlation between the vortex interaction and turbulent statistics and scalar statistics

According to the instantaneous vortex interaction (Fig. 11) and the production of spanwise and streamwise vorticity (the production represents the most common vortex interaction), there are mainly four kinds of vortex modes between the crests (R1-R4). To clearly show the correlation between the vortex interaction and the statistics of momentum and scalar, this section emphasizes the effect of vortex interaction on turbulent mass transfer.

Figure 13 shows the contours of turbulent statistics, including time-averaged streamwise and vertical velocities, turbulent kinetic energy (TKE), and Reynolds shear stress (RSS), as well as the isolines of spanwise and streamwise vorticity productions. Figures 13(a) and 13(b) show the momentum deficit caused by the flow separation behind the crest. After the flow reattaches on the windward side, the enhanced vertical velocity lifts the low momentum fluids, thus generating a wavy pattern of the low streamwise velocity. The high-level TKE and RSS above the trough indicate the formation of a turbulent shear layer [12]. Moreover, there is an apparent negative RSS on the windward side, which agrees with the results of related research [12,35]. The vortex structures are considered to be vital to generate the RSS feature [36,55].

The vortex production suggests that in the R1 region near the separation point, enhanced spanwise vorticity is located above and in front of the streamwise vortex, forming a complex shear with the streamwise vortices-induced vertical flow. These two interact and thus lead to the source of high TKE and RSS. In other words, the separated shear layer provides a shear effect on high TKE and RSS by a way which streamwise and spanwise vorticity interact. As shown in Figs. 13(c) and 13(d), the upwelling motion induced by the streamwise vortices lifts low-momentum fluid, and consequently, the vertical velocity fluctuation is negative. Meanwhile, the enhanced spanwise vorticity accelerates the upward flow, resulting in a positive streamwise velocity fluctuation. Hence, high positive TKE and RSS appear. In the R2 region, the recirculation motion of a separated bubble has an enclosed elliptical shape, crossed by $\bar{u} = 0$, and the velocity profiles above $\bar{u} = 0$ have features similar to those of the boundary layer flow. However, from $\bar{u} = 0$ to the wall boundary, the reversed velocity reaches a maximum at the midpoint between the wall and shear layer and decreases to zero approaching the wall. The strong convection above the SSL

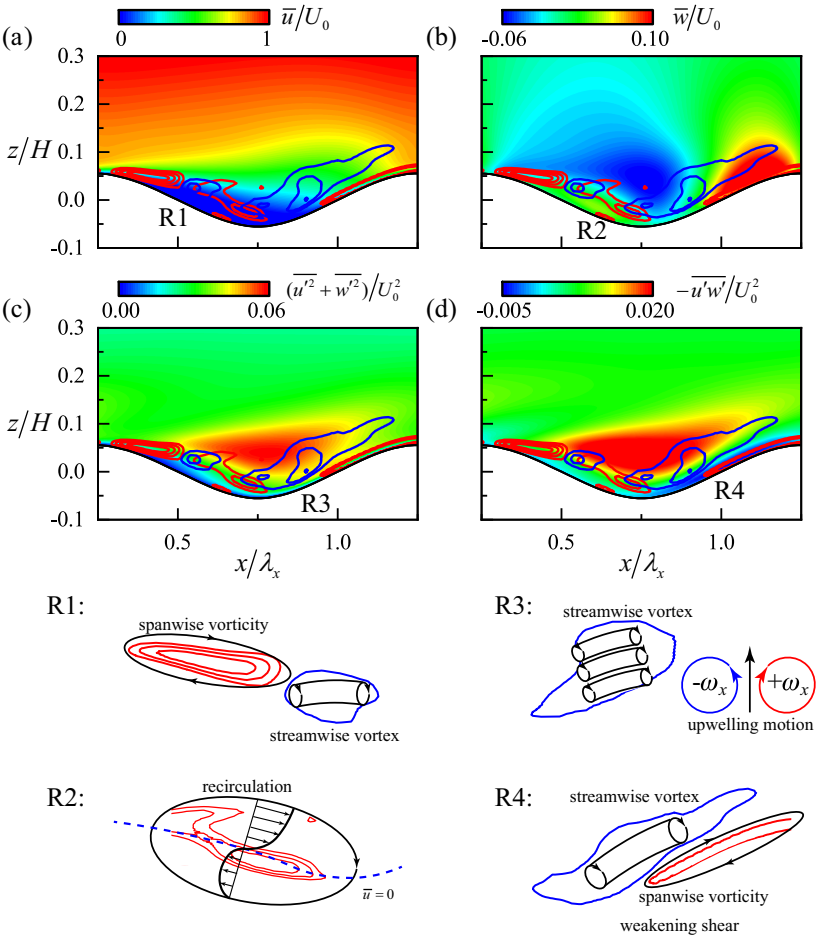

FIG. 13. Contours of (a) time-averaged streamwise velocity, (b) time-averaged vertical velocity, (c) turbulent kinetic energy (TKE), and (d) Reynolds shear stress (RSS) for case C3 and four vortex modes in regions R1–R4. The red solid line in the contour represents the spanwise vorticity production and the blue solid line represents the streamwise vorticity production. The blue dashed line for R2 represents $\bar{u} = 0$.

supports the production of turbulence. It is noted that in Fig. 4(c), at the trough near the separation bubble, a centrifugal instability may appear and develop streamwise vortices, but the recirculation motion of the separation bubble increases the streamwise velocity gradient in the near-wall region, with the viscous effect dominating the centrifugal effect. Therefore, streamwise vortices cannot be generated. This explains why the Görtler number is not high at the trough.

Streamwise vortices form continuously near the R3 region's reattachment point because of the high Görtler number. Vortex pairs in the streamwise direction provide upwelling motion and eject low-momentum fluid vertically into the average flow. This vertical motion is responsible for the wavy pattern of the streamwise velocity as shown in Fig. 13(a). In the R4 region on the windward side, the streamwise vortices produced at the latter origin rise to form a spatial layout in which spanwise vorticity has a downward distribution and streamwise vorticity has an upward distribution, which is reverse to the result in the R1 region. It is found that the streamwise flow above the spanwise vorticity interacting with the vertical flow between the streamwise vortices should lead to strong shear, but the RSS indicates a weakening shear owing to the reduction of the streamwise vorticity by the convex-wall effect (as shown in Fig. 7). Additionally, the negative RSS is highly related to

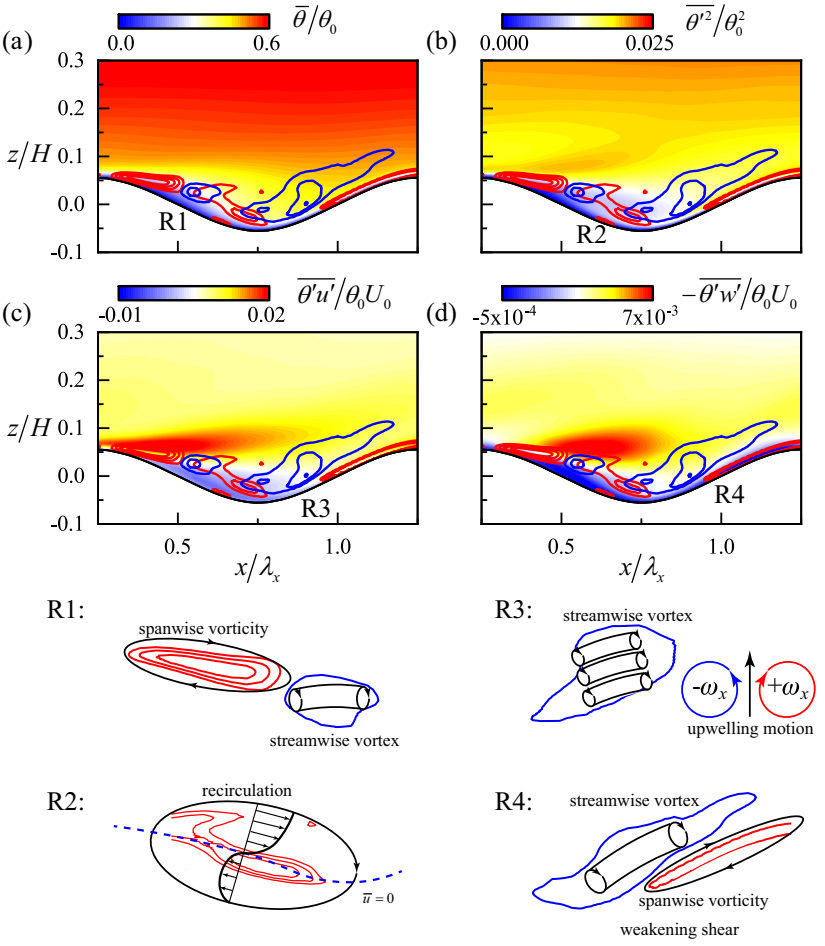

FIG. 14. Contours of (a) time-averaged scalar, (b) scalar variance, (c) streamwise turbulent scalar flux (STSF), and (d) vertical turbulent scalar flux (VTSF) for case C3.

the enhancement of the spanwise vorticity production, which is quite different from the results by Yang and Shen [36,55] who believed that the vertically bent quasistreamwise vortex dominates the negative RSS above waves.

To correlate the vortices production with the scalar transfer, Fig. 14 shows the scalar statistics and the corresponding four vortex interactions, including time-averaged scalar, scalar variance, streamwise turbulent scalar flux (STSF), and vertical turbulent scalar flux (VTSF). The wavy wall boundary enhances the scalar transport, as verified by Fig. 14(a) reveals an enhanced scalar transfer in the separation zone, with a lower scalar lifted to generate a lower scalar gradient. After the flow reattaches, a rapidly increased scalar gradient appears on the windward side due to the strong convection above the turbulent shear layer. A relatively high scalar variance originates upstream of the crest and vertically extends, as shown in Fig. 14(b), the extending feature is related to the recirculation motion of the separation bubbles. Therefore, scalar transfers without hindrance above the bubbles, whereas a lower level of scalar variance occurs within the separation zone, related to the lower level of turbulence in Fig. 13(c). The STSF in Fig. 14(c) suggests that high STSF also originates upstream of the crest and extends downstream which is parallel to the horizontal direction. This is because the streamwise fluctuating velocity changes the scalar fluctuations. But

the VTSF in Fig. 14(d) originates near the separation point. Moreover, the negative VTSF appears on both the leeward and windward sides. The former side is due to the effect of scalar diffusion, while the latter is attributed to the effect of scalar convection. This has been verified in our previous work through the variation of the Sherwood number [13].

The effect of vortex interaction on turbulent mass transfer is different from the momentum transport. In the R1 region, the interaction between spanwise and streamwise vorticity could not determine the origins of high scalar variance, STVF, and VTSF. The streamwise vortices-induced upwelling motion near the separation point is not vital in governing the origin of scalar statistics. As shown in Figs. 14(b)–14(d), high scalar variance, STVF, and VTSF originate at the crest where spanwise vorticity production enhances. Hence, the acceleration of streamwise flow caused by the spanwise vorticity increases the streamwise velocity fluctuation and thus scalar fluctuation. In other words, the scalar transfer is highly related to the streamwise momentum transfer. The mixed scalar in the R2 region is limited to the wall boundary, with the low momentum region trapped in the separation bubble; consequently, a scalar diffusion mechanism that is characterized by the Sherwood number dominates scalar transport on the leeward side [13]. Therefore, lower even negative scalar statistics appear.

The upwelling motion by the streamwise vortex pair lifts the low scalar fluid in the R3 region, where termination of high-order scalar statistics occurs. Distinct from the momentum transfer, the lifted scalar unaffected the time-averaged scalar in Fig. 14(a), that the high scalar featured with reversed wavy pattern compared with the streamwise velocity in Fig. 13(a). This arises because of the windward side's scalar convection-dominated mechanism. The strong convection above the turbulent shear layer is responsible for this variation. In the R4 region on the windward side, the interaction of spanwise and streamwise vorticity is similar in determining the statistics to that in Fig. 13. A convex wall provides a viscous effect sufficient to resist centrifugal instability and weakens streamwise vortices' development. Therefore, a weak shear between spanwise and streamwise vortices leads to the appearance of lower scalar statistics. It is noted that the enhanced spanwise vorticity production also contributes to the negative VTSF on the windward side.

Figure 15 gives the schematic diagram of wavy-wall-induced vortices and the corresponding effect on the high-order statistics of the momentum and scalar. On the windward side at $x/\lambda_x \approx 0.9$, the centrifugal instability induces the generation of streamwise vortices. The vortex structure extends downstream, gradually lifting away from the wall and forming a large angle in the horizontal direction. Beneath the vortex, the convex wall provides a viscous effect sufficient to resist centrifugal instability, limiting streamwise vortices' formation and development. However, the convex wall enhances the spanwise vorticity [as shown in Fig. 15(a)], and the increased spanwise vorticity develops into a spanwise vortex structure when divorcing from the crest downstream. Above the latter origin of the streamwise vortices, as shown in Figs. 15(b) and 15(c), the streamwise gradient of the vertical velocity decreases along the horizontal line AA'. Figures 15(f) and 15(g) show the quadrant distributions of the RSS and (VTSF on the windward side at $(x/\lambda_x, y/\lambda_x, z/H) = (1.1, 0, 0.025)$. Negative RSS appears in the region where the spanwise vorticity is enhanced (as shown by the red dashed line), which is dominated by events corresponding to turbulent ejection and sweep events. After the decomposition of velocity fluctuations, the streamwise velocity fluctuation appears with the same sign as the vertical velocity fluctuation. For the scalar quadrant, Q_{ts1} and Q_{ts3} events govern the negative VTSF, and the state $u' > 0$ ($u' < 0$) ensures positive (negative) values of scalar fluctuations.

Therefore, at the latter origin of streamwise vortices, the turbulent ejection and sweep events induced by the vortex pairs dominate the negative RSS, whereas downstream, the convex wall increases spanwise vorticity and leads to negative RSS. In the region of the interaction between streamwise vortices and enhanced spanwise vorticity, the RSS (VTSF) vertically converts from a negative value to a positive value.

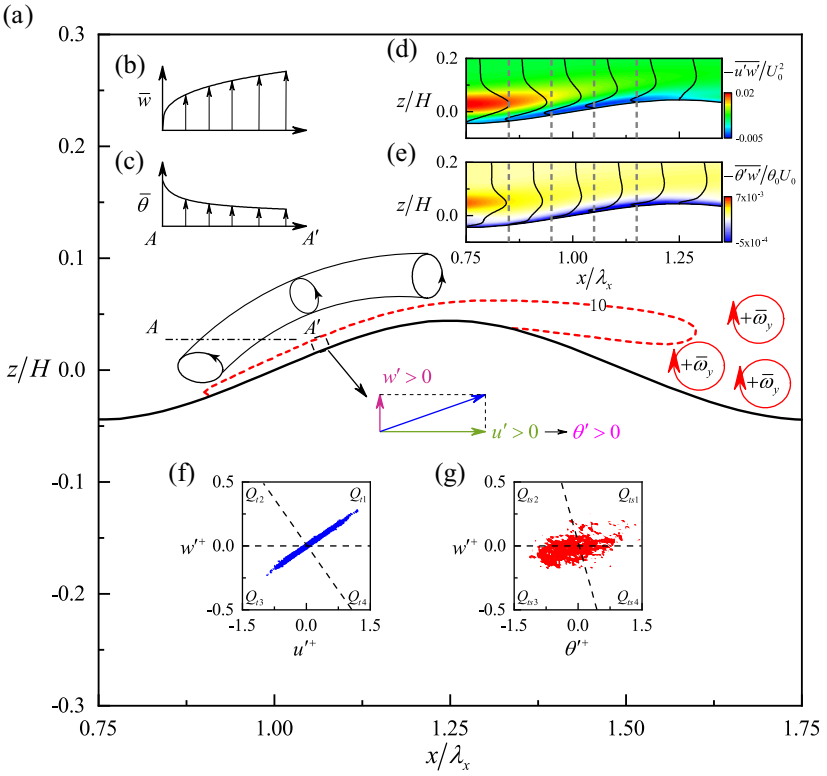

FIG. 15. (a) Schematic diagram of vortices induced by a wavy wall in case C2, with the red dashed line showing the isoline of $\bar{\omega}_y = 10$. Time-averaged (b) vertical velocity and (c) scalar along AA'. Contour and profiles of (d) RSS and (e) vertical turbulent scalar flux (VTSF). (f) Quadrant distribution of streamwise and vertical velocity fluctuations and (g) quadrant distribution of scalar and vertical velocity fluctuations on the windward side at $(x/\lambda_x, y/\lambda_x, z/H) = (1.1, 0, 0.025)$ [13,35].

VII. CONCLUDING REMARKS

The present paper investigated the generation and interaction of vortex structures induced by a two-dimensional wavy wall which is regarded as a large-scale obstacle based on the results of LES. Here, we considered the wave slope effect on the fully developed turbulent flow. A centrifugal instability is used to interpret the formation of the streamwise vortices, and then a vorticity production term is used to emphasize the generation of the spanwise vortices. After a comparison between these vorticity productions and statistics of momentum and scalar, how vortices interact to affect the turbulent mass transfer is summarized.

The present wavy wall induces flow separation, which reconstructs a turbulent shear layer having the same concave feature as the concave wall, triggering streamwise vortices through the centrifugal instability mechanism. We further confirmed that the separation and reattachment points are Görtler vortices' origins. However, the downstream convex wall provides a viscous effect sufficient to resist centrifugal instability, limiting the growth and evolution of streamwise vortices and consequently raising the vortices to form a typical vertically bent feature. The spanwise vortices are generated via the Kelvin-Helmholtz instability mechanism when it deviates from the crest. To emphasize the formation of the spanwise vortex, we calculated the spanwise component of the vorticity production using the vorticity transport equation. The production suggests that the growth of spanwise vorticity dominates the total production, whereas the strain effect-induced vorticity transformation

contributes only 4%. Hence, the spanwise vorticity is mainly generated by the growth of spanwise vorticity (the Kelvin-Helmholtz instability), but not the transformation from streamwise or vertical vortices.

The present wavy wall possesses four vortex modes between every two crests, which modulates the high-order statistics of turbulent mass transfer. The spatial layout of spanwise and streamwise vortices near the separation point leads to strong shear for producing high turbulent kinetic energy (TKE) and Reynolds shear stress (RSS), which is related to the streamwise vortices-induced upwelling motion and spanwise vorticity-induced acceleration of streamwise flow. However, the streamwise vortices induced-upwelling motion contributes rarely to the scalar variance, streamwise turbulent scalar flux (STSF), and vertical turbulent scalar flux (VTSF). Therefore, these scalar statistics originate upstream of the crest due to the spanwise vorticity-induced acceleration of streamwise flow. In the separation region, the separated shear layer (SSL) where the spanwise vorticity is produced provides a shear effect that maintains the trough's high TKE and RSS. However, the core enhancement of STSF and VTSF locate upstream of the trough, which is related to the trapped separation bubble-induced variation of scalar transfer. At the reattachment point, vortex pairs assembled by streamwise vortices that induce upwelling motion contribute slightly to the negative RSS and VTSF, whereas the enhanced spanwise vorticity through the activation of turbulent sweep and ejection events contributes momentously to the negative RSS and VTSF. On the windward side, the layout of spanwise and streamwise vortices is reversed to that near the separation point, and the restriction of the convex wall on the streamwise vorticity weakens the shear and generates low RSS and VTSF.

The present paper has discussed the vortex formation and interaction in a fully developed two-dimensional wavy wall turbulent mass transfer. However, some unresolved aspects still need further investigation. Firstly, the simplification of wind waves or naturally formed dunes as a two-dimensional wavy wall is not enough because of the wave's free surface and the dunes' geomorphology. The wind-wave dynamics are quite complex. Therefore, future investigation should consider the free surface effect of the waves. The naturally formed dunes are often three-dimensional large-scale terrains, affecting the above turbulent momentum transport in a more complicated way. The vortices in a three-dimensional wall are much more complex than the present study. Therefore, a detailed formation and evolution of vortices should be further investigated in a three-dimensional wavy wall. Moreover, a time-averaging field cannot reflect the instantaneous flow. The present time-averaged conduction represents the most common results in two-dimensional wavy wall turbulence, whereas the vortices are strongly time dependent. Therefore, the initial formation of the vortex structures and their evolution should be discussed in future investigations.

ACKNOWLEDGMENTS

The authors are grateful for the support from the National Natural Science Foundation of China (Grants No. 12032005, No. 12172057, and No.12002039). E.Z. thanks G. He for fruitful discussions.

[1] D. P. Zilker and T. J. Hanratty, Influence of the amplitude of a solid wavy wall on a turbulent flow. Part 2. Separated flows, J. Fluid Mech. **90**, 257 (1979).

[2] K. Krettenauer and U. Schumann, Numerical simulation of turbulent convection over wavy terrain, J. Fluid Mech. **237**, 261 (1992).

[3] Ch. Rapp and M. Manhart, Flow over periodic hills: An experimental study, Exp. Fluids **51**, 247 (2011).

[4] V. M. Segunda, S. J. Ormiston, and M. F. Tachie, Experimental and numerical investigation of developing turbulent flow over a wavy wall in a horizontal channel, Eur. J. Mech. B **68**, 128 (2018).

[5] D. P. Zilker and T. J. Hanratty, Influence of the amplitude of a solid wavy wall on a turbulent flow. Part 1. Nonseparated flows, J. Fluid Mech. **82**, 29 (1977).

[6] J. Buckles, T. J. Hanratty, and R. J. Adrian, Turbulent flow over large-amplitude wavy surfaces, J. Fluid Mech. **140**, 27 (1984).
[7] T. Nishimura, S. Murakami, S. Ararawa, and Y. Kawamura, Flow observations and mass transfer characteristics in symmetrical wavy-walled channels at moderate Reynolds numbers for steady flow, Int. J. Heat Mass Trans. **33**, 835 (1990).
[8] J. D. Hudson, L. Dykhno, and T. J. Hanratty, Turbulence production in flow over a wavy wall, Exp. Fluids **20**, 257 (1996).
[9] S. Nakagawa and T. J. Hanratty, Particle image velocimetry measurements of flow over a wavy wall, Phys. Fluids **13**, 3504 (2001).
[10] R. Kurose, T. Imashiro, and S. Komori, The effects of swell on turbulence over wavy walls, Int. J. Heat Fluid Flow **29**, 774 (2008).
[11] K. Chang, T. J. R. Hughes, and V. M. Calo, Isogeometric variational multiscale large-eddy simulation of fully-developed turbulent flow over a wavy wall, Comput. Fluids **68**, 94 (2012).
[12] A. M. Hamed, A. Kamdar, L. Castillo, and L. P. Chamorro, Turbulent boundary layer over 2D and 3D large-scale wavy walls, Phys. Fluids **27**, 106601 (2015).
[13] E. W. Zhang, X. L. Wang, and Q. Q. Liu, Numerical investigation on the temporal and spatial statistical characteristics of turbulent mass transfer above a two-dimensional wavy wall, Int. J. Heat Mass Trans. **184**, 122260 (2022).
[14] J. Jiménez, Turbulent flows over rough walls, Annu. Rev. Fluid Mech. **36**, 173 (2004).
[15] H. S. Yoon, O. A. El-Samni, A. T. Huynh, H. H. Chun, H. J. Kim, A. H. Pham, and I. R. Park, Effect of wave amplitude on turbulent flow in a wavy channel by direct numerical simulation, Ocean Eng. **36**, 697 (2009).
[16] H. M. S. Bahaidarah, N. K. Anand, and H. C. Chen, Numerical study of heat and momentum transfer in channels with wavy walls, Num. Heat Trans. A **47**, 417 (2006).
[17] I. P. Castro and A. Haque, The structure of a shear layer bounding a separation region. Part 2. Effects of free-stream turbulence, J. Fluid Mech. **192**, 577 (1988).
[18] C. J. Keylock, K. S. Chang, and G. S. Constantinescu, Large eddy simulation of the velocity-intermittency structure for flow over a field of symmetric dunes, J. Fluid Mech. **805**, 656 (2016).
[19] V. D. Angelis, P. Lombardi, and S. Banerjee, Direct numerical simulation of turbulent flow over a wavy wall, Phys. Fluids **9**, 2429 (1997).
[20] D. S. Henn and R. I. Sykes, Large-eddy simulation of flow over wavy surfaces, J. Fluid Mech. **383**, 75 (1999).
[21] A. Zenklusen, S. Kuhn, and P. R. von Rohr, Structural dissimilarity of large-scale structures in turbulent flows over wavy walls, Phys. Fluids **24**, 055112 (2012).
[22] B. Ničeno and E. Nobile, Numerical analysis of fluid flow and heat transfer in periodic wavy channels, Int. J. Heat Fluid Flow **22**, 156 (2001).
[23] C. C. Wang and C. K. Chen, Forced convection in a wavy-wall channel, Int. J. Heat Mass Transfer **45**, 2587 (2002).
[24] N. Kruse and P. R. von Rohr, Structure of turbulent heat flux in a flow over a heated wavy wall, Int. J. Heat Mass Tran. **49**, 3514 (2006).
[25] M. Omidyeganeh and U. Piomelli, Large-eddy simulation of two-dimensional dunes in a steady, unidirectional flow, JoT **12**, N42 (2011).
[26] R. A. Kostaschuk and M. A. Church, Macroturbulence generated by dunes: Fraser River, Canada, Sediment. Geol. **85**, 25 (1993).
[27] S. J. Bennett and J. L. Best, Mean flow and turbulence structure over fixed, two-dimensional dunes: Implications for sediment transport and bedform stability, Sedimentology **42**, 491 (1995).
[28] A. Müller and A. Gyr, On the vortex formation in the mixing layer behind dunes, J. Hydraul. Res. **24**, 359 (1986).
[29] S. Kuhn, S. Kenjereš, and P. R. von Rohr, Large eddy simulation of wall heat transfer and coherent structures in mixed convection over a wavy wall, Int. J. Therm. Sci. **49**, 1209 (2010).
[30] E. A. Zedler and R. L. Street, Large-eddy simulation of sediment transport: Currents over ripples, J. Hydraul. Eng. **127**, 444 (2001).

[31] M. Z. Hossain and A. K. M. S. Islam, Fully developed flow structures and heat transfer in sine-shaped wavy channels, Int. Commun. Heat Mass Trans. **31**, 887 (2004).
[32] S. Mahmud, A. K. M. S. Islam, and C. M. Feroz, Flow and heat transfer characteristics inside a wavy tube, Heat Mass Transfer **39**, 387 (2003).
[33] A. G. Ramgadia and A. K. Saha, Three-dimensional numerical study of turbulent flow and heat transfer in a wavy-walled duct, Int. J. Heat Mass Trans. **67**, 98 (2013).
[34] G. Z. Ma, C. X. Xu, H. J. Sung, and W. X. Huang, Scaling of rough-wall turbulence by the roughness height and steepness, J. Fluid Mech. **900**, R7 (2020).
[35] E. W. Zhang, X. L. Wang, and Q. Q. Liu, Effects of the spanwise heterogeneity of a three-dimensional wavy wall on momentum and scalar transport, Phys. Fluids **33**, 055116 (2021).
[36] D. Yang and L. Shen, Direct numerical simulation of scalar transport in turbulent flows over progressive surface waves, J. Fluid Mech. **819**, 58 (2017).
[37] P. Moin and J. Kim, Numerical investigation of turbulent channel flow, J. Fluid Mech. **118**, 341 (1982).
[38] Z. H. Xie, B. L. Lin, R. A. Falconer, and T. B. Maddux, Large-eddy simulation of turbulent open-channel flow over three-dimensional dunes, J. Hydraul. Res. **51**, 494 (2013).
[39] W. W. Kim and S. Menon, *A New Dynamic One-Equation Subgrid-Scale Model for Large Eddy Simulations*, 33rd Aerospace Sciences Meeting and Exhibit (AlAA, Reno, NV, 1995).
[40] T. Michioka, Large-eddy simulation for turbulent flow and gas dispersion over wavy walls, Int. J. Heat Mass Tran. **125**, 569 (2018).
[41] G. K. Batchelor, Small-scale variation of convected quantities like temperature in turbulent fluid. Part 1. General discussion and the case of small conductivity, J. Fluid Mech. **5**, 113 (1959).
[42] H. Tennekes and J. L. Lumley, *A First Course in Turbulence* (MIT, Cambridge, MA, 1972).
[43] S. Pirozzoli, M. Bernardini, and P. Orlandi, Passive scalars in turbulent channel flow at high Reynolds number, J. Fluid Mech. **788**, 614 (2016).
[44] D. Sipp and L. Jacquin, *A Criterion of Centrifugal Instabilities in Rotating Systems* (Springer, Berlin, 2000), p. 299.
[45] J. F. Beaudoin, O. Cadot, J. L. Aider, and J. E. Wesfreid, Three-dimensional stationary flow over a backward-facing step, Eur. J. Mech. B-Fluid. **23**, 147 (2004).
[46] O. Marxen, M. Lang, U. Rist, O. Levin, and D. S. Henningson, Mechanisms for spatial steady three-dimensional disturbance growth in a nonparallel and separating boundary layer, J. Fluid Mech. **634**, 165 (2009).
[47] M. Tobak, On Local Gortler Instability, ZAMP **22**, 130 (1971).
[48] G. R. Inger, *Spanwise-Periodic 3D Disturbances in the Wake of a Slightly Stalled Wing*, AlAA 25th Aerospace Sciences Meeting (AIAA, Reno, NV, 1987).
[49] J. Zhou, R. J. Adrain, S. Balachandar, and T. M. Kendall, Mechanisms for generating coherent packets of hairpin vortices in channel flow, J. Fluid Mech. **387**, 353 (1999).
[50] J. M. Floryan, On the Görtler instability of boundary layers, Prog. Aerospace Sci. **28**, 235 (1991).
[51] R. J. Calhoun and R. L. Street, Turbulent flow over a wavy surface: Neutral case, J. Geophys. Res. **106**, 9277 (2001).
[52] A. Benmalek and W. S. Saric, Effects of curvature variations on the nonlinear evolution of Goertler vortices, Phys. Fluids **6**, 3353 (1994).
[53] A. M. Hamed, M. Sadowski, Z. Zhang, and L. P. Chamorro, Transition to turbulence over 2D and 3D periodic large-scale roughnesses, J. Fluid Mech. **804**, R6 (2016).
[54] J. Jeong and F. Hussain, On the identification of a vortex, J. Fluid Mech. **285**, 69 (1995).
[55] D. Yang and L. Shen, Characteristics of coherent vortical structures in turbulent flows over progressive surface waves, Phys. Fluids **21**, 125106 (2009).